



ADDITIVE MANUFACTURING USING COMPOSITE POWDERS

Microstructural Characterization and Wear Resistance of 60 wt.%, 70 wt.%, and 80 wt.% WC-NiCrBSi Thin Walls Deposited Using Plasma Transferred Arc Additive Manufacturing

DYLAN ROSE ^{1,3} TONYA WOLFE,^{2,4} and HANI HENEIN^{1,5}

1.—Department of Chemical and Materials Engineering, University of Alberta, Edmonton, AB T6G 2H5, Canada. 2.—Centre for Innovation in Manufacturing, Red Deer Polytechnic, Red Deer, AB T4N 5H5, Canada. 3.—e-mail: drose1@ualberta.ca. 4.—e-mail: tonya.wolfe@rdpolytech.ca. 5.—e-mail: hhenein@ualberta.ca

Plasma transferred arc additive manufacturing (PTA-AM) was used to deposit 60 wt.%, 70 wt.%, and 80 wt.% WC-NiCrBSi metal matrix composites. The 60 wt.% samples had a homogeneous distribution of WC particles. At 70 wt.% and 80 wt.%, two defects were found in the microstructure: areas completely void of WC, termed denuded regions, and large pores. The microstructure of the 60 wt.% sample consisted of blocky complex carbides [(Ni₄W₂Cr₂Si)C₃], γ -Ni cellular dendrites, a halo around the primary dendrites, and a lamellar eutectic of Ni₃Si/Ni₃B. There is increased thermal degradation of WC at 70 wt.% WC, causing a wider array of complex carbides and higher W contents in the γ -Ni dendrites and the halo. Thermo-calc software was used to model the solidification of NiCrBSi with 10 wt.% W to determine the effect that W addition has on the solidification of the Ni alloy, and the results were compared to the 60 wt.% and 70 wt.% WC-NiCrBSi PTA-AM deposits. The abrasive wear resistance and the impact resistance of 60 wt.%, 70 wt.%, and 80 wt.% WC deposited with PTA-AM were comparable to a 60 wt.% WC-NiCrBSi PTA overlay.

INTRODUCTION

Industries ranging from agriculture^{1–3} to pipelines^{4–6} and mining^{7–9} encounter abrasive wear provoking environments. The Canadian Energy Sector incurs losses in the billions of dollars annually due to the replacement of damaged components that have failed because of abrasive wear.¹⁰ To mitigate the issue, traditional methods, such as material substitution, surface treatments, and overlaying equipment with a hard metal or some form of metal matrix composite (MMC), are used. An MMC consists of a tough metal matrix with a homogenous distribution of a hard reinforcement phase, usually in the form of chromium (e.g., Cr₃C₂)^{11–13} or tungsten carbide (WC).^{14–16} Currently, NiCrBSi embedded with 65 wt.% WC overlayed using plasma

transfer arc (PTA) offers the best wear resistance in mining applications with severe abrasion and impact wear.^{14,17} In PTA, a plasma arc is struck between a substrate and a tungsten electrode, and the material is mechanically fed into the arc and deposited onto the substrate material. Under conventional PTA conditions, the Ni matrix solidifies as primary γ -Ni dendrites, with Ni/Ni₃B eutectic.^{10,15,17} The high heat input from conventional PTA causes convective mass transfer of W and C from the WC particles, reducing the erosion and corrosion resistance of the overlay.^{15,18,19} The introduction of W and C into the matrix causes the formation of high W-containing intermetallics throughout the Ni matrix, including Cr₃C₂, Cr₇C₃, and Ni₂W₄C or W₂C (β) polymorphs and α -WC.^{10,17,19,20}

Plasma transferred arc additive manufacturing (PTA-AM) is an advanced metal additive manufacturing technology that uses a plasma arc as a heat source to deposit material in a layer-by-layer

(Received March 16, 2023; accepted August 9, 2023; published online September 5, 2023)

fashion. It is a variant of the more commonly known method of PTA welding, but with the added capability of building up complex shapes in three dimensions. PTA-AM is capable of printing customizable material compositions at build rates up to 2.1 kg/h, making it an ideal deposition modality for the large parts required for the Canadian Energy Sector.²¹ When depositing Ni-based super alloys using PTA-AM, the microstructure consists of Ni dendrites that grow epitaxially from the substrate and the previously deposited material. Precipitation of MC and $M_{23}C_6$ have been found in the interdendritic regions. A change in growth direction for the topmost layers cause there to be anisotropic mechanical properties.^{22,23} PTA-AM has also been used for the deposition of stainless steel,^{24,25} tool steel,²⁶ and titanium alloys.^{27,28} There has been limited research carried out on PTA-AM of WC-NiCrBSi MMCs. Rojas et al.²⁹ altered the operating parameters during PTA-AM of a 60 wt.% WC-NiCrBSi MMC, and found that the overall microstructure contained WC, γ -Ni, Ni_3Si , Ni_3B , and $Cr_{23}C_6$. This varies from the microstructure obtained using a laser heat source, where the microstructure contained γ -Ni dendrites, γ -Ni + Ni_3B eutectic, $Cr_{23}C_6$, Ni_3Fe , $Ni_{31}Si_{12}$, and CrB.³⁰ The phases present in the microstructure do not suggest the degree of carbide dissolution that is experienced during PTA-AM, which could be attributed to the low heat input. However, no compositional analysis was carried out on the various phases of the microstructure to confirm the extent of the dissolved W in the matrix.

The present study aims to investigate how increasing the WC content from 60 wt.% to 70 wt.% and 80 wt.% in WC-Ni MMCs affects the distribution of carbides, formation of complex carbides, solidification structure of the matrix, and resistance to abrasive wear. The solidification of the MMC was modeled using Thermo-calc's Scheil solidification simulation, which was compared to the microstructure from the PTA-AM deposits. The effects of varying levels of W in the matrix on the solidification sequence of the microstructure is discussed. Additionally, the abrasive wear resistance and impact resistance of 60 wt.%, 70 wt.%, and 80 wt.% WC-NiCrBSi PTA-AM deposit are compared with a 60 wt.% WC-NiCrBSi PTA overlay.

MATERIALS AND METHODS

Thermodynamics of WC-NiCrBSi

To understand the solidification sequence of the phases present in the microstructure of the PTA-AM of WC-NiCrBSi, Thermo-calc (v2022b, TCNI12 database) thermodynamic software was used. Thermo-calc results provide a framework for the thermodynamic and microstructural literature available for the WC-NiCrBSi system. The solidification simulations were carried out on the Ni

matrix with the addition of 10 wt.% W, to provide an understanding of how the addition of W affects the microstructure of the NiCrBSi matrix. It should be noted that the average overall W content found in the Ni-matrix from the PTA-AM of 70 wt.% WC-NiCrBSi was ≈ 7.7 wt.% (≈ 2.0 at%), and that no carbon was included in the thermodynamic calculations due to the low solubility (2.8 at%) of C in Ni.³¹ Additionally, with the addition of C in the Scheil calculation, Thermo-calc always forms WC. Removing C would force W to be in a solid solution with Ni and the W in the matrix phases could be compared with PTA-AM. Scheil solidification was chosen as it is one of the limiting conditions in solidification. The concentration of the solute can be determined using:

$$C_s = kC(1 - V_s)^{(k-1)} \quad (1)$$

where C_s is the concentration of the solid, k is the partition coefficient, V_s is the volume fraction of solid that has formed, and C is the nominal composition of the alloy.

Plasma Transferred Arc Additive Manufacturing

The PTA-AM experiments were carried out using a Stellite Starweld 300 M constant current power source with a Stellite Excalibur PTA torch. A 4.8-mm thoriated-tungsten electrode with a 4-mm setback was used, as recommended by the manufacturer. The electrode tip angle was maintained between 10° and 20°. The current, voltage, travel speed, and powder flow were set to 37 A, 20 V, 600 mm/min, and 27 g/min, respectively. For comparison, the current, voltage, travel speed, and powder flow used for conventional PTA overlays are 130 A, 24 V, 230 mm/min, and 27 g/min, respectively. It should be noted that the current is set based on the PTA controller dial, which is analog and was calibrated within the range of 100–200 A. The values used in this experiment were lower than the calibrated region and a linear extrapolation may not be valid. The energy density was calculated by dividing the power (current \times voltage) by the powder feed rate. The contrast in the energy density (6.9 kJ/g for overlays and 1.6 kJ/g for AM) would create different thermodynamic conditions and resultant microstructure between the two methods. This reinforces the need for a complete microstructural analysis of the WC-Ni system under AM conditions. The powder used for deposition was a blend of WOKA Durit 6030 and Kennametal SCNC070 monocrystalline WC, whose composition and size range is shown in Table I. To build the single-track, multi-layer walls, the torch oscillated using the built-in gantry system with a width of 27 mm, and the height was adjusted manually to maintain a constant voltage. At the end of each layer, a dwell time of 0.4 s was used to ensure an even layer height. The Ni-WC MMC was deposited

Table I. Composition and size of the matrix material used in this work

Matrix material	Composition (wt.%)							Size range (μm)
	Ni	Cr	B	Si	W	C	Fe	
WOKA Durit 6030	Bal	5.0–6.5	0.8–1.2	3.8–4.3	–	0.2–0.5	< 1.5	+63–180
Kennametal SCNC070 monocrystalline	–	–	–	–	93.6	6.4	–	+63–180

onto sand-blasted 12.7-mm-thick (1/2") mild steel substrates with no pre-heat.

Infrared Imaging

A Mikron M7640 infrared camera was used to monitor the build's temperature to determine the effects of balling on the part's thermal history. The infrared camera has a temperature range of 0–2000°C and is equipped with a 640×480 focal plane array microbolometer with a spectral bandwidth of 8–14 μm . The emissivity was not measured during the deposition, and during the experiment, the emissivity was set to 1. Therefore, the infrared results were used as qualitative observations to compare the heat build-up. LumaSpec™ Offline Analyzer 5.0 software was used to set the range of temperatures recorded to be from 200°C to 700°C to reduce the saturation of the images.

Characterization

An in-depth characterization of the microstructure of 60 wt.% and 70 wt.% WC in a NiCrBSi matrix was conducted. The optical microscopy images were taken using an Olympus PMG3 optical microscope, and images were captured using an Olympus Q color 5 camera with Quartz PCI V5 software. Scanning electron microscopy (SEM) was used to characterize the solidification structure of the PTA-AM deposits. The SEM used in this work was a Tescan Vega 3 equipped with a thermal emission source. The microstructure was imaged using an accelerating voltage of 20 keV and a working distance of 15 mm. The SEM also contains an Oxford election dispersive spectroscopy (EDX) system which was used to acquire semi-quantitative compositional data of all of the phases in the microstructure. All compositional data in this section are an average of 10 data points. The phase distribution was determined using a Zeiss Sigma field-emission SEM equipped with an AZtechSynergy electron backscatter diffraction (EBSD) detector.

Wear and Impact Testing

The abrasive wear and impact resistance of the 60 wt.%, 70 wt.%, and 80 wt.% WC-NiCrBSi PTA-AM samples were tested and compared with a conventional overlay. Testing the performance was

a means of determining if adding more WC would lead to superior properties. Wear performance was determined using a dry sand, rubber wheel abrasion test, following procedure A in the ASTM G65-16 standard. The sand in the Athabasca oil sands are generally angular quartz particles, 95% of which are less than 150 μm .³² The sand particles ranged from 50 to 70 mesh (297–210 μm), and the size of the test coupon was 25.4 mm \times 76.2 mm \times 12.7 mm. Procedure A, which is a 6000-revolution test as outlined in the ASTM standard, was carried out twice per sample. The first test is to remove any of the softer surface matrix material and expose the carbides underneath. The second test is performed on the scar from the first test to mimic steady-state wear conditions. The impact test is a non-standardized test developed by Fisher et al. for testing the impact resistance of overlays for oilsands applications.³³ The test coupon was 25.4 \times 69.9 \times 12.7 mm and was struck by an S2 tool steel hammer at 150 rpm, creating an impact of approximately 8 J. The test was run for 3-min intervals and the coupon was weighed before and after each interval, for 24 min or until failure. A rotary impact test was chosen to understand the material's resistance to repeated low-energy impacts and is a routine test for characterizing overlays in the oil sands mining sector.

RESULTS

Thermodynamic Evaluation of WC-NiCrBSi

A Scheil solidification simulation was carried out on the NiCrBSi matrix with 10 wt.% W (Fig. 1) and the composition of the different phases are found in Table II. Primary solidification begins with γ -Ni solid solution at (\approx 1220°C), containing W, Si, Cr, and Fe. Since the TCNI12 database only contains binary and ternary thermodynamic data, the decrease in the melting point could be due to error in the extrapolation to a 6-element system. The equilibrium partition coefficient for W, Cr, and Fe in the presence of Ni and Si are 2.0, 1.1, and 1.1, respectively.³⁴ The reductions in W, Cr, and Fe in γ -Ni as solidification progresses follow the values of the partition coefficients.³⁴ The Ni₃Si phase had trace amounts of Cr and Fe, while the Ni₃B phase contained the highest amounts of Cr, Fe, and B. Additionally, there is the formation of WB during the solidification of Ni₃Si/Ni₃B.

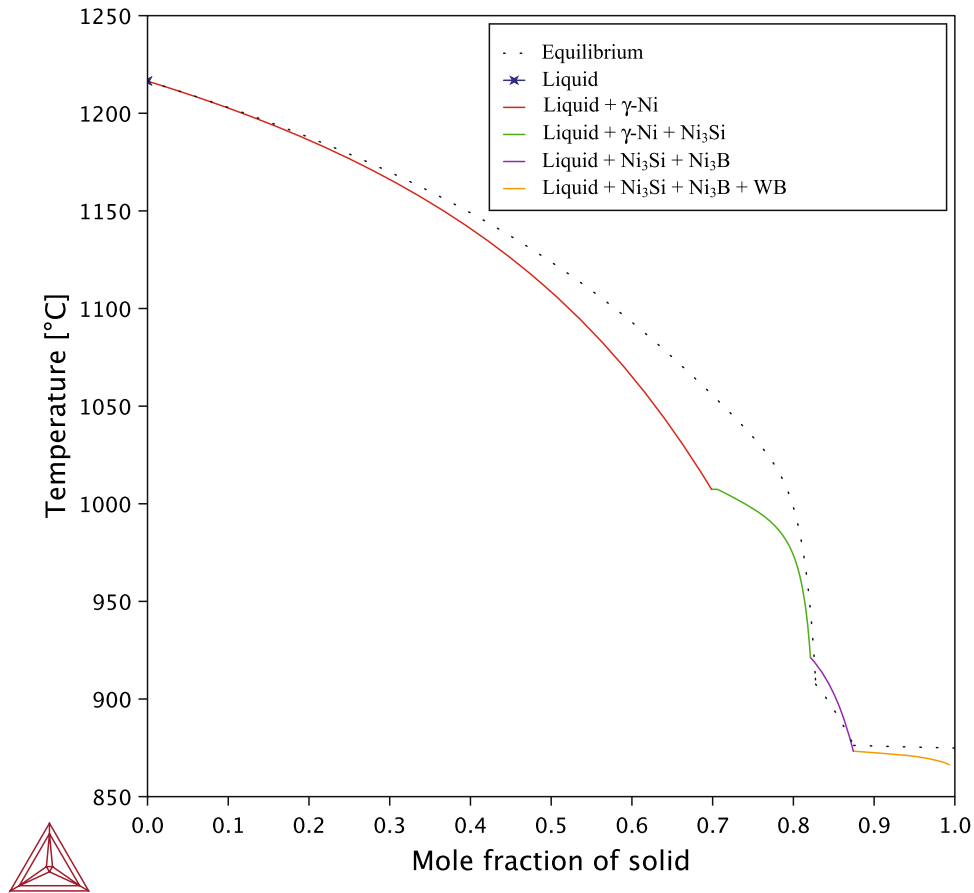


Fig. 1. Scheil solidification simulation of Durit 6030 NiCrBSi matrix with 10 wt.% W. The compositions for the different phases are provided in Table II.

Table II. The composition of the different phases shown in Fig. 1 using Thermo-calc

Phase	at%					
	Ni	W	Si	Cr	Fe	B
γ-Ni	81.5–80.2	1.4–0.5	10.0–13.0	6.3–5.7	0.8–0.6	–
Ni ₃ Si	75.4	–	23.5	0.9	0.2	–
Ni ₃ B	63.1–64.2	–	–	9.0–8.5	2.9–2.3	25.0
WB	–	51.8–55.7	–	–	–	48.2–44.3

The range of values highlights the difference in composition as solidification progresses, where the first and last numbers are the composition at the beginning and end of solidification, respectively. If no range is given the composition was constant.

PTA-AM: Comparison Between 60 wt.%, 70 wt.%, and 80 wt.% WC

The as-built samples for the 60 wt.%, 70 wt.%, and 80 wt.% monocrystalline WC are shown in Fig. 2, and the sample dimensions are 90 mm × 27 mm × 6 mm, 75 mm × 27 mm × 8 mm, and 65 mm × 27 mm × 9 mm for the height, length, and thickness, respectively. Comparing the builds in Fig. 2, the higher loading of WC increased the surface roughness of the wall. The 60 wt.% WC wall

had more slumping during the deposition, denoted by the inconsistent layer geometry (red arrows in Fig. 2a). The red square at the bottom of the samples in Fig. 2 shows that the first few layers have a slightly different texture and layer geometry. Instead of being a uniform stringer bead, the first layer was discontinuous balls; this is known as the “balling effect” and is a common defect in AM.^{35–37} The balling effect is due to insufficient wetting^{37–39} of the MMC with the substrate due to the lack of substrate pre-heat, and low heat input from the

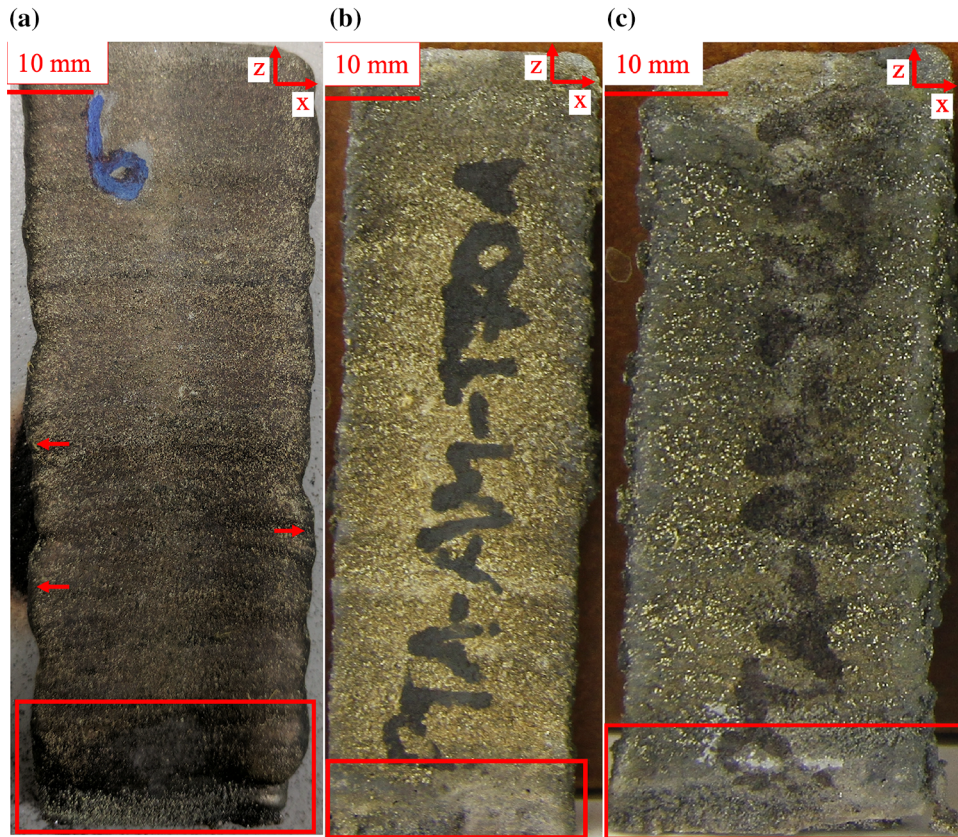


Fig. 2. PTA-AM samples containing 60 (a), 70 (b), and 80 (c) wt.% monocrystalline WC in a Durit 6030 NiCrBSi matrix. The sample dimensions for (a), (b), and (c) are 90 mm \times 30 mm \times 6 mm, 75 mm \times 27 mm \times 8 mm, and 65 mm \times 27 mm \times 9 mm, respectively. The writing on the samples are identification numbers and should be ignored (Color figure online).

plasma. Once sufficient heat had been supplied, the MMC was uniformly deposited. The balling effect is exacerbated by the increased carbide content, which could be due to the reduced flowability of the melt,⁴⁰ and an increase in the effective viscosity.⁴¹ The balling effect can cause discontinuities in the build in each subsequent layer.²⁹ In some cases, the space between the balling is filled in by the liquid, but in others, the error cascades through the rest of the build. The observation of balling is also a sign of poor bonding with the substrate, which would decrease the heat transfer efficiency between the substrate and the part.

An infrared camera was used to monitor the heat accumulation during the PTA-AM build process and are shown in Fig. 3. Note that these walls differ from those shown in Fig. 2 and the uneven build height is due to poor operating conditions. Increasing the energy density has been previously shown to increase the wetting of the newly deposited material and decrease the balling effect.^{35,42,43} For Fig. 3a and d, the current was increased to 95 A for the first 5 layers and then decreased to 37 A. Samples A and C could be removed manually with ease, while the higher current samples were metallurgically

bonded. Comparing the thermal profile from Fig. 3a and b, as well as Fig. 3c and d, it can be seen that the bonding with the substrate drastically changes the amount of heat that is retained during printing. For the 60 wt.% sample, the average temperature in the sample decreased and significantly more heat was transferred to the substrate based on the increase in substrate temperature. The effects of adding 10 wt.% more WC on the thermal history is plainly shown when comparing Fig. 3a and b with Fig. 3c and d. The 70 wt.% samples had more heat accumulation than the 60 wt.% samples, which could be attributed to the difference in thermal properties between the two deposits. The heat capacity for Ni and WC at 200–700°C is 7.8–8.0 J/molK⁴⁴ and 27.6–36.0 J/molK,⁴⁵ respectively. Additionally, the thermal conductivity of Ni is 90⁴⁶ and WC is 110⁴⁷ W/mK. With the heat capacity and thermal conductivity of WC being higher than Ni, the more WC content in the sample, the more heat that will be accumulated in the sample. The significant amount of porosity in the sample (Fig. 4) would lead to poor heat transfer through the wall, which could contribute to the higher amounts of heat accumulation.

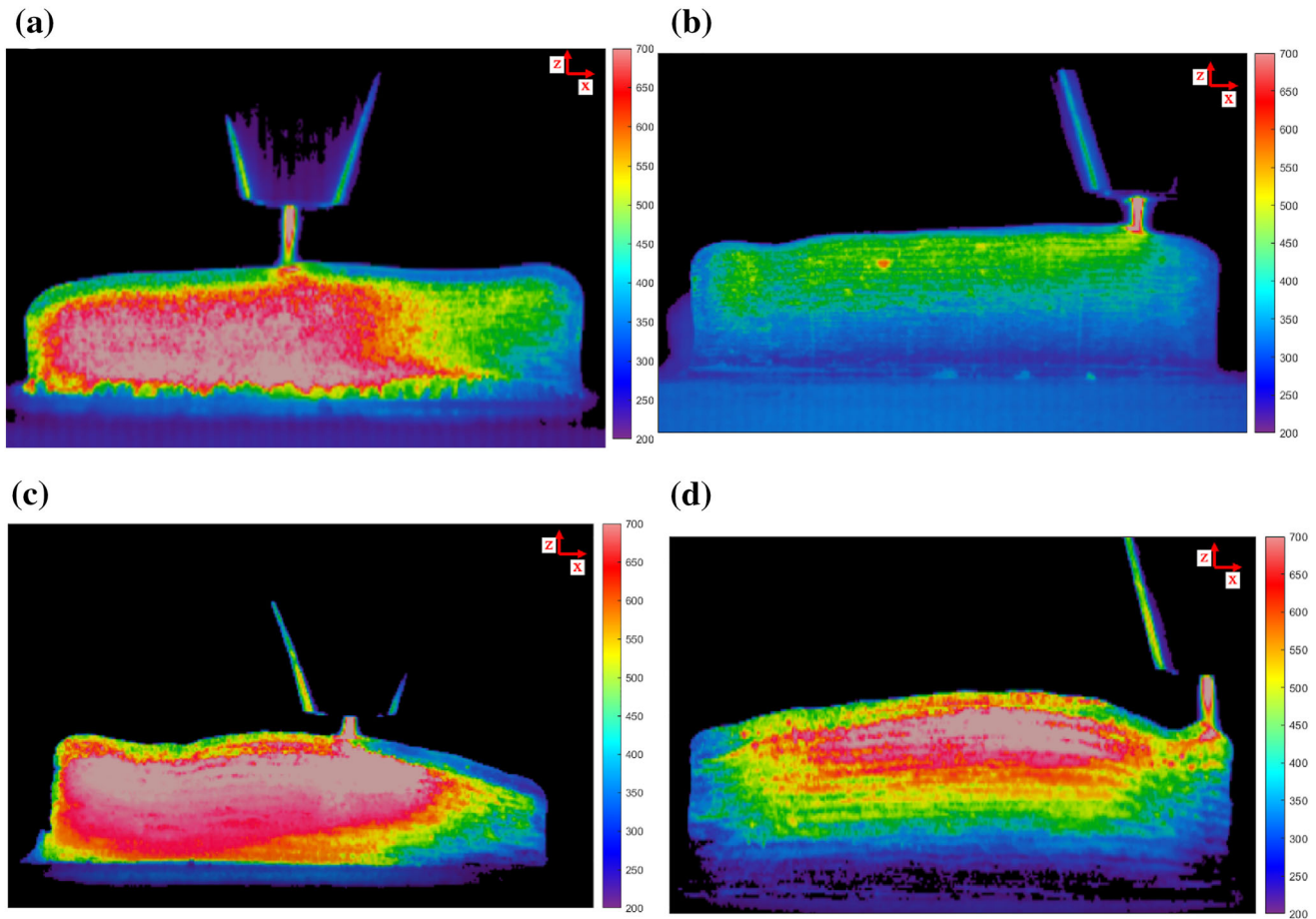


Fig. 3. (a) 60 wt.% WC with constant 37A current, (b) 60 wt.% starting at 95A current, then dropping to 37A after 5 layers, (c) 70 wt.% WC with constant 37A current, and (d) 70 wt.% starting at 95A current, then dropping to 37A after 5 layers. The sample dimensions for (a), (b), (c), and (d), are 100×26 mm, 100×25 mm, 100×26 mm, and 100×35 mm, respectively. Note that the torch oscillates back and forth in the x-direction.

Microstructural Characterization

Microstructural Comparison of 60 wt.%, 70 wt.%, and 80 wt.% WC in NiCrBSi

The microstructure of the 60 wt.%, 70 wt.%, and 80 wt.% WC in a NiCrBSi matrix are shown in Fig. 4a, b, and c, respectively. The 60 wt.% sample had a homogeneous distribution of WC particles with very little porosity. With an additional 10 wt.% and 20 wt.% WC, two defects dominate the microstructure: areas void of WC, termed denuded regions¹⁷ (labeled in Fig. 4c), and large pores. Due to the undesirable microstructure obtained from both 70 wt.% WC and 80 wt.% WC, 80 wt.% WC was not considered for further analysis. The large pores were speculated to be a result of different mechanisms. The large irregular-shaped pores could be manufacturing defects resulting from sub-optimal deposition parameters and from poor flowability of the melt pool from increased apparent viscosity.⁴¹ There has not been any confirmed mechanism that causes denuded region formation. Sundaramoorthy et al. proposed that denuded regions could be from liquid Ni forming in the plasma not mixing with the remainder of the

melt pool due to surface tension.¹⁰ Wolfe et al. suggests that W vapor formed in the plasma may diffuse into Ni droplets and enter the pool as a mushy phase.¹⁷ The mushy spheres would then retain their spherical shape during solidification. Backscatter SEM was used to observe the microstructure of 60 wt.% monocrystalline WC in NiCrBSi matrix, shown in Fig. 5. The monocrystalline WC are the large white angular particles. The build direction did not play a role in the microstructure that was obtained. There were three primary morphologies of secondary carbides that formed during solidification, which include blocky carbide (A), small blocky carbides (B), and ring carbides (C), shown in Fig. 5b. The Ni matrix formed a cellular dendritic structure (D), most of which contained a halo (E) surrounding the dendrite shown in Fig. 5c. The interdendritic region contains a lamellar eutectic (F). Previous literature states that the eutectic of 60 wt.% WC in NiCrBSi consists of γ -Ni and Ni_3B .^{10,20,48} When a laser heat source is used for the deposition, the eutectic structure is lamellar.^{49,50} A phase with a ring-like morphology (G) can also be found throughout the microstructure, and, based on the cracks seen as

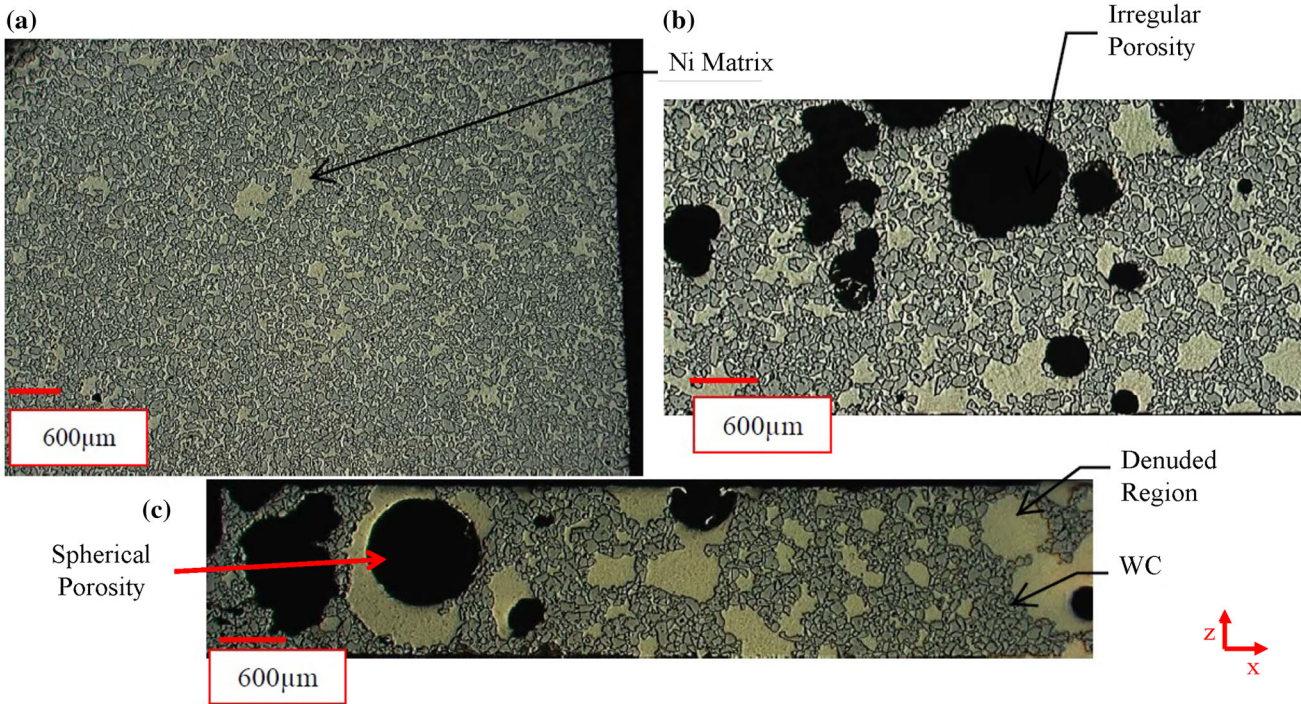


Fig. 4. Optical microscopy images of the microstructures from the samples shown in Fig. 2, where (a) is 60 wt.% WC, (b) is 70 wt.% WC, and (c) is 80 wt.% WC. The light green is the Durit 6030 matrix, the dark green particles are WC, and the black regions within the sample are pores (Color figure online).

the black lines in the red square in Fig. 5d, this phase is likely brittle. The cracks form when the ring phase is in close proximity to a WC particle, and could be due to thermal residual stresses during solidification.^{51,52}

The composition of the different phases are located in Table III. It should be noted that carbon is below the detection limit of EDX, so the carbon content is likely incorrect. Since no W is found in the matrix alloy, one of the mechanisms that could introduce W to the microstructure is convective mass transfer from the WC during the PTA-AM deposition process. Convective mass transfer from WC during PTA is a common phenomenon.^{10,16,17,19,20} The brighter phases have a higher molecular weight, highlighting the distribution of W throughout the microstructure. Convective mass transfer of W and C resulted in three different morphologies of secondary complex carbide particles (A, B, and C) containing varying amounts of alloying elements. The larger blocky carbides (A) had higher W, C, and Cr content ($(\text{Ni}_4\text{W}_2\text{Cr}_2\text{Si})\text{C}_3$), while the smaller (B) ones had a higher Ni and Si content ($(\text{Ni}_3\text{WCrSi})\text{C}_2$). The ring carbides (c) tend to have the highest Ni and lowest W content ($(\text{Ni}_8\text{W}_4\text{Cr}_3\text{Si}_2)\text{C}_6$) of all of the carbides.

The primary phase (D) is a Ni solid solution containing W, Si, Cr, and Fe. The halo (E) around the primary phase contains no W, less Cr and Fe, and more Si. The equilibrium partition coefficient for W, Cr, and Fe in the presence of Ni and Si are 2.0, 1.1, and 1.1, respectively.³⁴ In contrast, the

partition coefficient for Si is around 0.5. It should be noted that the equilibrium partition coefficient would be affected by the interaction between the alloying elements, and by the change in the solidification temperature caused by the alloying additions.³⁴ However, the distribution of the alloying elements in the Ni matrix is supported by the ternary equilibrium partition coefficients.³⁴ The primary phase that solidifies first has higher concentrations of W, Cr, and Fe than phases that form later in the solidification process (from the remaining liquid after forming the primary phase). The light phase in the lamellar eutectic (F) has less Si and slightly higher levels of Cr compared to the dark phase. The lamellar spacing is $1.04\ \mu\text{m}$, and the interaction volume for the emission of characteristic X-rays in iron is approximately $1\ \mu\text{m}^3$.⁵³ Therefore, it is possible that some of the detected characteristic X-rays from the dark phase of the eutectic are included in the signal from the light phase of the eutectic, and vice versa. This would mean that the Si content in the light phase and the Cr content in the dark phase could be overestimated. The ring phase (G ($(\text{Ni}_4\text{WCr}_{13}\text{Si})\text{C}_{10}$)) contained all of the alloying elements except for Fe.

Characterization of 70 wt.% WC in NiCrBSi

A low-magnification backscatter SEM image mainly of a denuded region in a 70 wt.% angular monocrystalline WC in NiCrBSi is shown in Fig. 6a.

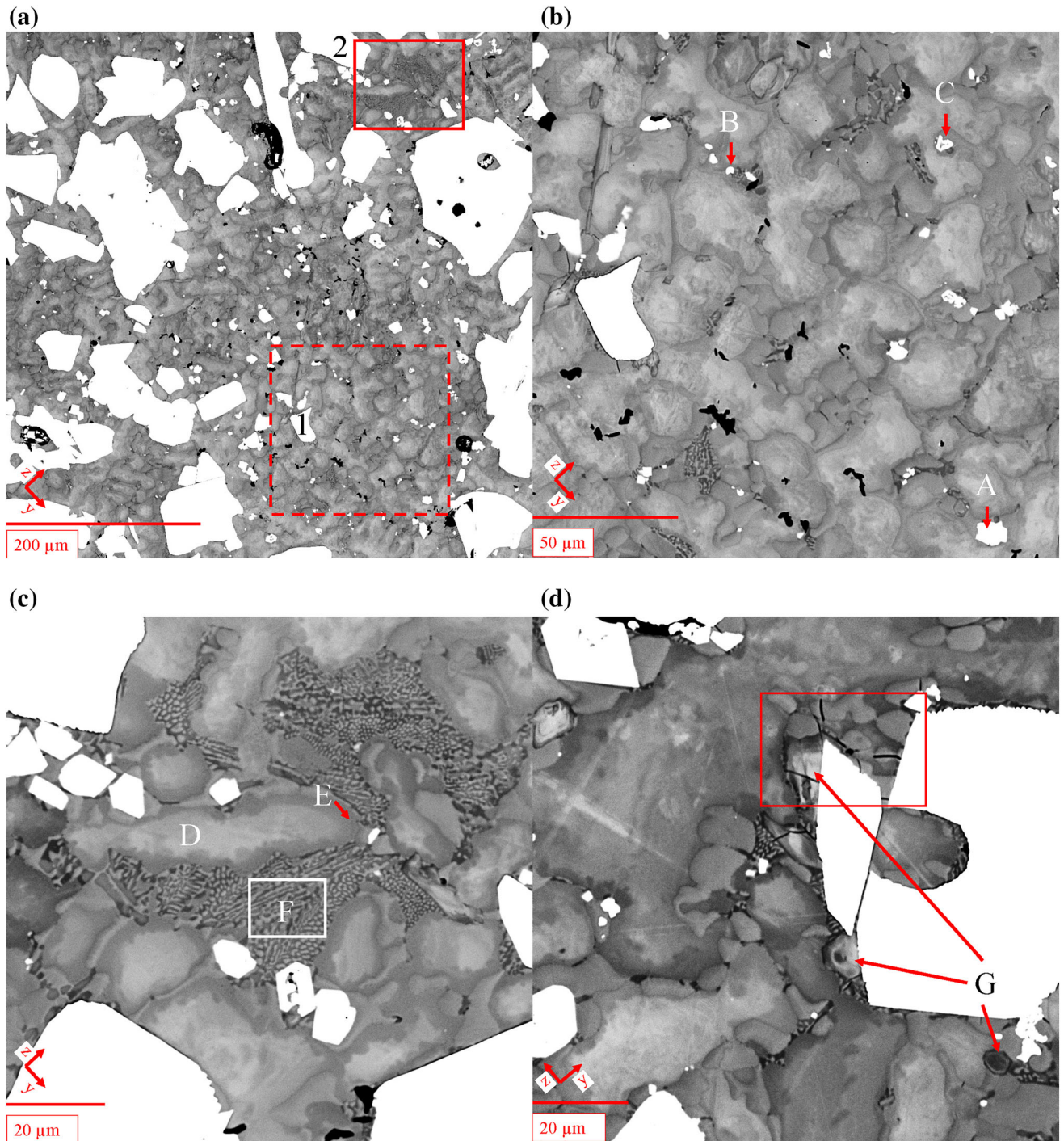


Fig. 5. Backscatter SEM images of 60 wt.% WC-NiCrBSi MMCs where (a) is a overview of the microstructure; (b) the dashed red square (1) in (a); (c) the red square (2) in (a); (d) phases that form around a WC particle. The phases with a higher molecular weight are shown as brighter. The letters correspond to the compositions presented in Table III (Color figure online).

Higher magnification images of the microstructure are presented in Fig. 6b, c, and d. The monocrystalline WC are the large white angular particles.

The convective mass transfer of W and C from the WC is evident by the abundance of secondary W phases growing on the monocrystalline WC, shown in Fig. 6b.^{48,54–56} The W and C dissolved in the Ni matrix resulted in different morphologies of

secondary carbide phases, such as star carbides (A), needle carbides (B), and blocky carbides (C). The Ni matrix contains a primary dendritic phase (D), most with halos (E) around the primary phase, similar to what is found at 60 wt.% WC. The interdendritic region contains a lighter gray phase (F), and a darker gray phase (G). There are regions where there is eutectic growth (H and I).

Table III. The composition of the different phases shown in Fig. 5 using EDX

Letter	Description	PTA-AM (at%)						Thermo-calc (at%)					
		Ni	W	Si	C	Cr	Fe	Ni	W	Si	Cr	Fe	B
A	Blocky carbide	31.2	17.7	8.2	22.3	20.6	–	–	51.8– 55.7	–	–	–	48.2– 44.3
B	Small blocky carbide	37.8	18.3	13.3	30.0	15.3	–	–	51.8– 55.7	–	–	–	48.2– 44.3
C	Ring carbide	42.9	21.4	11.0	17.4	17.3	–	–	51.8– 55.7	–	–	–	48.2– 44.3
D	Primary phase	82.1	2.4	6.7	–	6.2	2.6	81.5– 80.2	1.4–0.5	10.0– 13.0	6.3– 5.7	0.8– 0.6	–
E	Halo around primary phase	85.5	–	10.2	–	4.2	2.1	–	–	–	–	–	–
F	Eutectic: light phase	85.7	–	9.9	–	3.0	1.3	63.1– 64.2	–	–	9.0– 8.5	2.9– 2.3	25.0
	Eutectic: dark phase	80.7	–	16.8	–	2.0	1.2	75.4	–	23.5	0.9	0.2	–
G	Ring phase	11.2	3.6	3.8	38.8	45.8	–	–	51.8– 55.7	–	–	–	48.2– 44.3

The range of values provided by Thermo-calc highlights the difference in composition as solidification progresses, where the first and last numbers are the composition at the beginning and end of solidification, respectively. If no range is given the composition was constant. Note that the compositions provided are averaged from multiple points and may not sum to 100%.

Additionally, there is a ring-shaped carbide (J) found in the interdendritic regions.

The composition of the different phases are shown in Table IV. The secondary carbide phases all contained varying amounts of W, C, and Cr, with the star morphology (A) containing the most W ($(\text{Ni}_3\text{W}_3\text{Cr}_6)\text{C}_6$), and the ring phase (J) having the most Cr ($(\text{Ni}_2\text{WCr}_9)\text{C}_9$). The blocky carbide phase (C) had small amounts of Si detected ($(\text{Ni}_4\text{W}_2\text{Cr}_2\text{Si})\text{C}_3$). The W primary M characteristic X-ray and Si primary K_α have an energy of 1.774 keV and 1.739 keV, respectively. The similar magnitude of characteristic X-rays makes them difficult to distinguish during EDX analysis. In the presence of Si, W's L_α peak of 8.396 keV helps to distinguish between the two. Si only has the single L_α peak that is detectable with EDX; therefore, the Si content could be influenced by the presence of W. The primary phase (D) of the Ni matrix had a higher W and Cr content but lower Si content than the halo (E) surrounding the primary phase. Having higher concentrations of Cr and W in the primary phase is supported by the equilibrium partition coefficient being greater than unity in the presence of Si.³⁴ In the interdendritic region, the phases contained higher levels of Si and lower levels of Cr and Fe. The composition of the light interdendritic phase in the non-lamellar (F) and lamellar (H) structures are slightly different, due to the elevated Si content in the lamellar structure. The average lamellar spacing is 1.02 μm for 70 wt.% WC-NiCrBSi, and the interaction volume for the emission of characteristic X-rays in iron is approximately 1 μm^3 .⁵³ Therefore, it is possible that some of the detected characteristic X-rays from phase I was included in the signal from

phase H causing elevated levels of Si and reduced levels of Cr and Fe. Based on the EDX compositional data, it is possible that the light (F and H) dark phases (G and I) are the same phase.

EBSD was used to determine the phase distribution in 70 wt.% monocrystalline WC in NiCrBSi, as seen in Fig. 7. The image is 200 \times 200 pixels with a step size of 1 μm . The blue phase is γ -Ni, the red phase is Ni_3B , the yellow phase is WC, and the teal phase is W_2C . None of the black pixels were able to be classified. $\text{Ni}_3\text{W}_3\text{C}$ was included in the phase database during data collection, but was not contained within the sample. Ni_3Si was also included, but due to the similarity in cell spacing between Ni (0.345 nm) and Ni_3Si (0.351 nm), Ni_3Si was unable to be distinguished from Ni. It was found that the halo around with primary phase was also γ -Ni. The interdendritic regions contained mostly Ni_3B , and γ -Ni. The large step size of 1 μm would not be able to resolve the eutectic, resulting in just γ -Ni or Ni_3B being detected. Additionally, the needle phase (B) was found to be W_2C , which forms in the interdendritic regions and around the edge of the primary WC. Although the composition of the needle phase measured with EDX (B in Table IV) contains Cr and Ni, the EBSD results are based on crystal structure and not composition.

DISCUSSION

Solidification of WC-NiCrBSi

60 wt.% WC-NiCrBSi

From the SEM images (Fig. 5), the solidification sequence for 60 wt.% WC-NiCrBSi can be hypothesized. Due to their high W content, the first phases

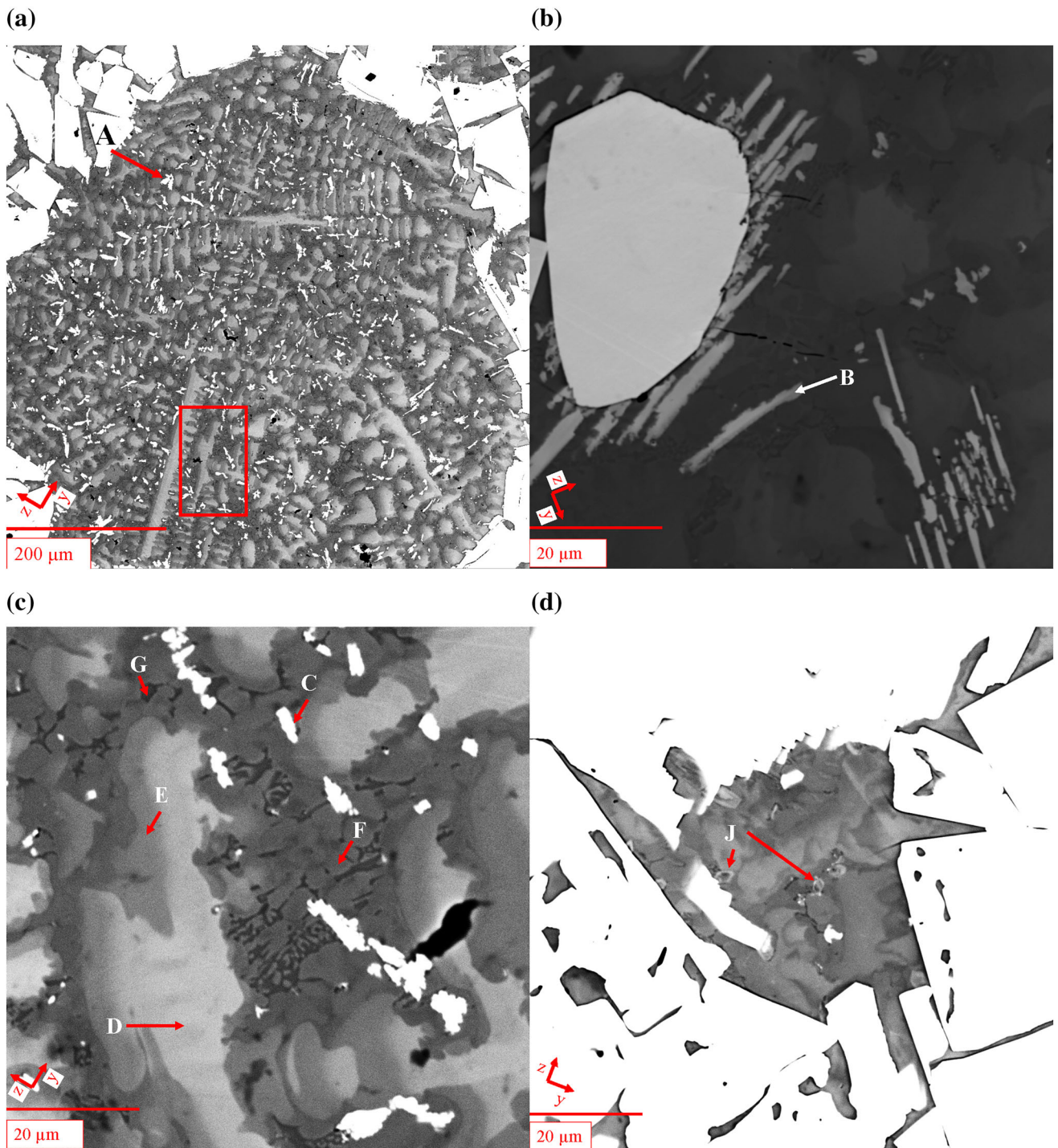


Fig. 6. Backscatter SEM images of 70 wt.% WC-NiCrBSi MMC where (a) is a microstructural overview of a denuded region; (b) secondary carbide phases around WC particles; (c) the red square in (a) showing higher magnification of the matrix; (d) the ring phases found in the microstructure. The heavier elements are shown as brighter highlighting the distribution of W throughout the sample. The letters correspond to the compositions presented in Table IV (Color figure online).

to form are likely the secondary carbide phases (Table IIIA–C). Additionally, Cr_3C_2 's (Table IIIG) found in the interdendritic regions likely form prior to γ -Ni since the melting point of Cr_3C_2 is 1900°C .⁵⁷ Following the formation of the high W phases, the primary γ -Ni phase (Table IIID) forms. Dendrite

coring could cause there to be micro segregation in the dendrites as they grow, resulting in a difference in composition during the primary solidification. The higher levels of W, Cr, and Fe in the primary phase are supported by the partition coefficients being higher than unity.³⁴ Therefore, it could be

that the formation of the halo (Table IIIID) is due to dendrite coring. The continued growth of the primary phase would then bring the composition of the liquid to the eutectic composition, after which there is eutectic growth of Ni and Ni₃B (Table IIIIF).

70 wt.% WC-NiCrBSi

The SEM, EDX, and EBSD data can be used to estimate the solidification sequence for 70 wt.% WC-NiCrBSi. Due to their high W content, the first phases to form are the different varieties of secondary carbide phases (Table IVA–C) found in the microstructure. Based on the composition, it is difficult to determine the order the secondary carbides form due to their similarities in W content. The next phase that forms could be the CrC (Table IVJ) since the melting point of Cr₃C₂ is 1900°C.⁵⁷ After the carbides have formed, the first Ni phase to form would be the primary dendritic phase (Table IVD). The halo surrounding the primary dendrites (Table IVE) could be due to dendrite coring during primary solidification. After the formation of the halo, the next phase to form is the eutectic solidification of Ni₃B and a Ni-Si solid solution.

Comparing Thermo-calc to PTA-AM

A comparison of the compositions from the Thermo-calc (Fig. 1) simulations and the PTA-AM of 60 (Fig. 5a) and 70 wt.% WC (Fig. 6a) are shown in Tables III and IV, respectively. The solidification sequence proposed by the Scheil solidification simulation from Thermo-calc (Fig. 1) does have some resemblance to what is experienced during PTA-

AM. In Thermo-calc and PTA-AM, the solidification of the matrix begins with the primary solidification of a γ -Ni solid solution. In the Scheil simulation, the composition of the alloying elements varies as solidification progresses. The composition of the alloying elements in the primary phase for the 60 wt.% and 70 wt.% WC samples under PTA-AM are outside of the compositional ranges simulated by Thermo-calc. The Cr, W, and Fe contents are higher, while the Si content is lower in PTA-AM compared to Scheil solidification.

Where Thermo-calc deviates from PTA-AM is not including the solidification of the halo. In the 60 wt.% (Fig. 5c) and 70 wt.% WC (Fig. 6c), there is generally a distinct line between the primary phase and the halo. It is likely that the halo is the continued growth of the primary phase at a different composition. In the Scheil solidification simulation, the formation of the halo should be a separate phase that is formed after γ -Ni solidification. The lack of halo formation would contribute to the compositional differences of the other phases between PTA-AM and Scheil (Tables III and IV). The Ni₃Si formation prior to the formation of the eutectic is also not representative of PTA-AM. The solidification of the Ni₃Si/Ni₃B is in agreement with what is found in PTA-AM, although the compositions are different. The last phase to form is WB in the Scheil solidification, which could be the tiny white spherical spots in the eutectic in Fig. 6c. TEM could be carried out on the eutectic to confirm whether the white points in the eutectic are WB. The Scheil solidification simulations are a good tool for attempting to understand the solidification sequence of the NiCrBSi matrix in PTA-AM, but the rapid solidification conditions of PTA-AM are different than Scheil resulting in major microstructural differences. Additionally, since the TCNI12 database only contains binary and ternary thermodynamic data, the extrapolations that are made to a 6-element system could be incorrect and result in a difference in the composition of the predicted phases.

Microstructural Comparison Between 60 wt.% and 70 wt.% WC in NiCrBSi

From the compositional data gathered using EDX (Tables III and IV), increasing the WC content from 60 wt.% to 70 wt.% appears to increase the amount of thermal degradation of WC. The secondary dendrite arm spacing (SDAS) was measured to estimate the cooling rate for 60 wt.% and 70 wt.% WC. It was found that the locations in the sample shown in Fig. 5a (60 wt.%) and Fig. 6a (70 wt.%) had a SDAS of 11.5 ± 2.0 and 12.7 ± 2.4 μ m, respectively. With the significant overlap of the standard deviations, it was assumed that the cooling rates at these two locations were similar. The area fraction of secondary carbides were compared between Figs. 5a and 6a and it was found that the

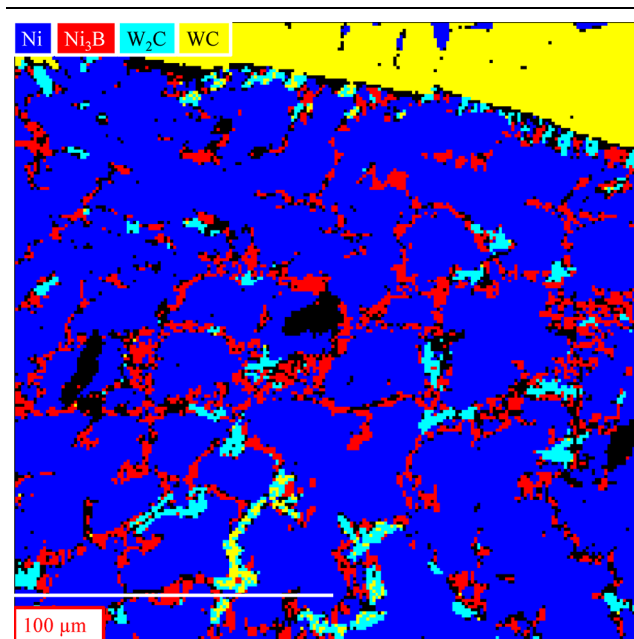


Fig. 7. Phases detected using EBSD, where blue is Ni, red is Ni₃B, yellow is WC, and teal is W₂C. The grid is 200 × 200 pixels with a step size of 1 μ m (Color figure online).

Table IV. The composition of the different phases shown in Fig. 6 using EDX

Letter	Description	PTA-AM (at%)						Thermo-calc (at%)					
		Ni	W	Si	C	Cr	Fe	Ni	W	Si	Cr	Fe	B
A	Star carbide	6.1	19.5	–	35.9	38.5	–	–	51.8– 55.7	–	–	–	48.2– 44.3
B	Needle carbide	13.2	14.2	–	35.9	36.7	–	–	51.8– 55.7	–	–	–	48.2– 44.3
C	Blocky carbide	31.0	18.8	7.9	22.7	19.6	–	–	51.8– 55.7	–	–	–	48.2– 44.3
D	Primary phase	83.5	3.3	6.1	–	7.2	3.0	81.5– 80.2	1.4–0.5	10.0– 13.0	6.3– 5.7	0.8– 0.6	–
E	Halo around primary phase	81.1	1.8	8.3	–	6.0	2.9	–	–	–	–	–	–
F	Eutectic: light phase (NL)	91.5	–	3.8	–	4.6	1.7	63.1– 64.2	–	–	9.0– 8.5	2.9– 2.3	25.0
G	Eutectic: dark phase (NL)	77.7	–	17.8	–	3.1	1.3	75.4	–	23.5	0.9	0.2	–
H	Eutectic: light phase (L)	82.4	–	12.3	–	3.7	1.6	63.1– 64.2	–	–	9.0– 8.5	2.9– 2.3	25.0
I	Eutectic: dark phase (L)	78.8	–	17.4	–	2.9	1.0	75.4	–	23.5	0.9	0.2	–
J	Ring phase	7.8	4.8	–	44.3	43.1	–	–	51.8– 55.7	–	–	–	48.2– 44.3

The range of values provided by Thermo-calc highlights the difference in composition as solidification progresses, where the first and last numbers are the composition at the beginning and end of solidification, respectively. If no range is given the composition was constant. For the eutectic NL stands for non-lamellar and L stands for lamellar.

60 wt.% sample had a secondary carbide area fraction of 2.9% while the 70 wt.% samples was 4.28%. The semi-quantitative EDX measurements show that there is more W in the primary phase of the 70 wt.% sample (Table IV) and W present in the halo around the primary phase. No W exists in the halo around the primary phase in the 60 wt.% WC sample (Table III). Therefore, with a higher volume fraction of secondary carbide phases and higher levels of W in the Ni matrix, it is deduced that the 70 wt.% WC did have higher levels of convective mass transfer of W. Comparing the microstructure of 60 wt.% and 70 wt.% WC is thus determining the effect W has on the microstructure of rapidly solidified NiCrBSi.

Adding more dissolved W in the matrix causes significant changes to the overall microstructure. The 70 wt.% samples had a wider array of secondary carbides that formed, as opposed to the 60 wt.% samples that contained mainly the large blocky morphology ((Ni₄W₂Cr₂Si)C₃). The large blocky morphology ((Ni₄W₂Cr₂Si)C₃) was still present in the 70 wt.% sample with similar composition. However, the ring carbide (C ((Ni₈W₄Cr₃Si₂)C₆)) in Fig. 5b) was not found in the 70 wt.% sample. In the 70 wt.% samples, the secondary carbides are finer plates in a needle ((NiWCr₃)C₃) or star ((NiW₃Cr₆)C₆) morphology, with higher concentrations of Cr. The difference in the secondary carbide morphology may be

attributed to the increase in the dissolved W and C in the Ni matrix from the increased convective mass transfer. Additionally, the carbides in the 70 wt.% samples tended to have more W and Cr than those found in the 60 wt.% sample. Both samples formed a high Cr (CrC) ring phase that is typically found in close proximity to the WC particles. This could be due to the convective mass transfer of C from the WC particles reacting with the Cr in the Ni solution to form the high Cr carbides.

One of the significant differences between the 60 wt.% and 70 wt.% WC samples was the structure of the Ni matrix. The 70 wt.% sample showed more obvious dendritic structure, than the 60 wt.% sample. The primary γ -Ni dendrites in the 70 wt.% sample had more dissolved W (9.9 wt.%) than those found in the 60 wt.% sample (7.5 wt.%). The difference in W content is due to the increased thermal degradation of WC in the 70 wt.% sample. The higher W content in Ni could result in a finer Ni structure. Both samples had halos that formed around the primary γ -Ni dendrites. The halo in 60 wt.% WC has no W, while the halo for 70 wt.% WC had 5.9 wt.% W. The increased convective mass transfer of W caused W to be rejected from the primary phase into the liquid, which is then retained in the halo phase. Additionally, the contrast of the halo compared to the primary dendrite in Fig. 5c supports that W is likely not present in

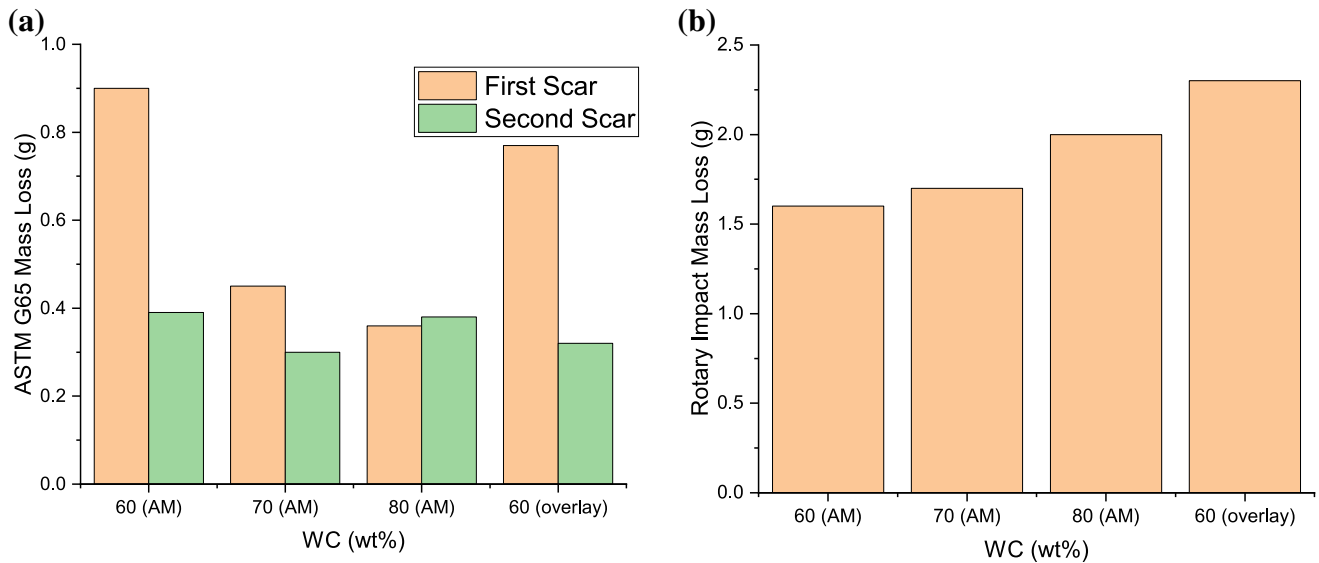


Fig. 8. (a) and (b) are the results comparing the samples shown in Fig. 2 and a 60 wt.% overlay for ASTM G65 and rotary impact test, respectively.

the halo in the 60 wt.% sample. The halo for the 70 wt.% sample has more Cr and Fe, and less Si. There have been no studies on the effect of W on the partitioning of Cr and Fe in Ni. In ternary Ni-5Si-3W alloys, W does not affect the partition coefficient of Si compared to Ni-5Si.³⁴ However, this may change with higher W content. The halo formation in both the 60 wt.% and 70 wt.% samples is postulated to be from dendrite coring causing continued growth of the primary phase at a different composition.

The interdendritic regions for 60 wt.% have a higher tendency to be a lamellar eutectic. In 70 wt.% WC, the increased W content appears to reduce the amount of lamellar eutectic found. However, drawing any conclusions from a 2-D cross-section of the microstructure is difficult. Additionally, the eutectic structure could be too fine to be resolved using SEM and may require higher magnification techniques like TEM. A better understanding of the differences in the eutectic structure could be established using serial sectioning using a focused ion beam SEM (FIBSEM). Using FIBSEM, a 3-D rendering of the entire microstructure could be created and a more thorough comparison of the microstructure between 60 wt.% and 70 wt.% WC could be conducted.

Wear and Impact Testing

The results from the ASTM G65 tests are shown in Fig. 8a. The lower first scar mass loss from the higher WC samples is likely due to the higher amount of WC on the surface of the sample, shown by the rough surface in Fig. 2. Based on the second scar mass loss, the AM samples had comparable abrasive wear resistance under the test conditions. Additionally, the AM samples performed slightly

better in the repeated rotary impacts, as presented in Fig. 8b. For the case of 70 wt.% and 80 wt.%, even with the manufacturing defects and denuded regions, the abrasive wear and impact resistance were similar to 60 wt.% overlays. This implies that with the removal of these defects, the performance may surpass conventional overlays. However, the displayed results are from a single sample, and more tests would be required to definitively compare the performance of AM and conventional WC-Ni MMCs.

CONCLUSION

PTA-AM was used to deposit thin walls of a 60 wt.%, 70 wt.%, and 80 wt.% WC-NiCrBSi metal matrix composite. Increasing the WC content from 60 wt.% to 70 wt.% caused large irregular and spherical-shaped pores and denuded regions. The increased WC content also caused more thermal degradation of the WC, causing more W and C to be dissolved in the Ni matrix. Having more W dissolved in the Ni matrix caused precipitation of more complex carbides, higher levels of W in the Ni dendrites and halo. The Scheil solidification simulations did not include the solidification of the halo around the primary phase. The difference between the Scheil simulations and PTA-AM samples highlights the need for more thermodynamic and microstructural characterization data that need to be generated for the NiCrBSi-WC system. The abrasive and impact resistance are comparable between the 60 wt.%, 70 wt.%, and 80 wt.% PTA-AM samples, and the 60 wt.% overlay, showing that the superior abrasive wear resistance of WC-NiCrBSi overlays could be applied to additively manufactured parts.

ACKNOWLEDGEMENTS

The research conducted in this study was made possible through the financial support from the Syncrude-NSERC CRD (CRDPJ 514752-17) and HI-AM (NSERC HI-AM NETGP 494158). The authors would like to thank Stefano Chiovelli for his continued support throughout the conduction of this work. A special thank you to Innotech Alberta for supplying the PTA and consumable for this project.

CONFLICT OF INTEREST

On behalf of all authors, the corresponding author states that there is no conflict of interest.

REFERENCES

1. A.S. Alwan, *Eng. Technol. J.* 32(9), 2205 (2014).
2. J. Votava, *J. Central Eur. Agric.* 15(2), 119 <https://doi.org/10.5513/JCEA.V15I2.2647> (2014).
3. A.H. Jones and P. Roffey, *Wear* 267(5), 925 <https://doi.org/10.1016/j.wear.2009.01.042> (2009).
4. M.A. Islam and Z.N. Farhat, *Wear* 311(1–2), 180 <https://doi.org/10.1016/J.WEAR.2014.01.005> (2014).
5. O.E. Adedeji, L. Zhang, D.E.S. Breakey, and R.S. Sanders, *Wear* 477, 203767 <https://doi.org/10.1016/J.WEAR.2021.203767> (2021).
6. L. Ba, Q. Gao, W. Cen, J. Wang, and Z. Wen, *Vacuum* 192, 110427 <https://doi.org/10.1016/J.VACUUM.2021.110427> (2021).
7. A.I. Gusev, N.A. Kozyrev, A.A. Usoltsev, R.E. Kryukov, and A.R. Mikhno, *IOP Conf. Ser. Earth Environ. Sci.* 206(1), 012034 <https://doi.org/10.1088/1755-1315/206/1/012034> (2018).
8. M. Petrica, E. Badisch, and T. Peinsitt, *Wear* 308(1–2), 86 <https://doi.org/10.1016/J.WEAR.2013.10.005> (2013).
9. L. Xu, C. Vose, and D. StJohn, *Wear* 162–164(PART B), 820 [https://doi.org/10.1016/0043-1648\(93\)90083-X](https://doi.org/10.1016/0043-1648(93)90083-X) (1993).
10. R. Sundaramoorthy, S.X. Tong, D. Parekh, and C. Subramanian, *Wear* 376–377, 1720 <https://doi.org/10.1016/j.wear.2017.01.027> (2017).
11. M.C. Carvalho, Y. Wang, J.A.S. Souza, E.M. Braga, and L. Li, *Eng. Fail. Anal.* 60, 374 <https://doi.org/10.1016/j.engfailanal.2015.11.058> (2016).
12. L. Ma, C. Huang, J. Jiang, R. Hui, Y. Xie, and Z.-S. Liu, *Eng. Fail. Anal.* 31, 320 <https://doi.org/10.1016/j.engfailanal.2013.01.050> (2013).
13. N. Barnes, S. Borle, and P.F. Mendez, *Sci. Technol. Weld. Join.* 22(7), 595 <https://doi.org/10.1080/13621718.2017.1278831> (2017).
14. M. Jones and U. Waag, *Wear* 271(9), 1314 <https://doi.org/10.1016/j.wear.2011.01.046> (2011).
15. A. Neville, F. Reza, S. Chiovelli, and T. Revega, *Wear* 259(1), 181 <https://doi.org/10.1016/j.wear.2005.02.037> (2005).
16. T. Liyanage, G. Fisher, and A.P. Gerlich, *Wear* 274–275, 345 <https://doi.org/10.1016/j.wear.2011.10.001> (2012).
17. T. Wolfe, Homogeneity of Metal Matrix Composites Deposited by Plasma Transferred Arc Welding. *PhD Thesis*. University of Alberta, Edmonton (2010). <https://doi.org/10.7939/R3K64Q>.
18. Z. Kamdi, P.H. Shipway, K.T. Voisey, and A.J. Sturgeon, *Wear* 271(9), 1264 <https://doi.org/10.1016/j.wear.2010.12.060> (2011).
19. G. Fisher, T. Wolfe, and K. Meszaros, *J. Therm. Spray Technol.* 22(5), 764 <https://doi.org/10.1007/s11666-012-9877-4> (2013).
20. T. Liyanage, G. Fisher, and A.P. Gerlich, *Surf. Coat. Technol.* 205(3), 759 <https://doi.org/10.1016/j.surfcoat.2010.07.095> (2010).
21. T. Lehmann, D. Rose, E. Ranjbar, M. Ghasri-Khouzani, M. Tavakoli, H. Henein, T. Wolfe, and A.J. Qureshi, *Int. Mater. Rev.* 67(4), 410 <https://doi.org/10.1080/09506608.2021.1971427> (2022).
22. E.A. Alberti, B.M.P. Bueno, and A.S.C.M. D'Oliveira, *Int. J. Adv. Manuf. Technol.* 83(9–12), 1861 <https://doi.org/10.1007/s00170-015-7697-7> (2016).
23. E.M. Perez-Soriano, E. Ariza, C. Arevalo, I. Montealegre-Melendez, M. Kitzmantel, and E. Neubauer, *Metals* 10(2), 200 <https://doi.org/10.3390/met10020200> (2020).
24. S. Moghazi, T. Wolfe, D. Ivey, and H. Henein, *Int. J. Adv. Manuf. Technol.* **In press** (2020).
25. M. Dalaei, F. Cheaitani, A. Arabi-Hashemi, C. Rohrer, B. Weisse, C. Leinenbach, and K. Wegener, *Int. J. Adv. Manuf. Technol.* 106(9), 4375 <https://doi.org/10.1007/s00170-019-04917-2> (2020).
26. S.H. Nikam and N.K. Jain, *Int. J. Adv. Manuf. Technol.* 95(9), 3679 <https://doi.org/10.1007/S00170-017-1472-X> (2017).
27. S. Ríos, P.A. Colegrove, and S.W. Williams, *J. Mater. Process. Technol.* 264, 45 <https://doi.org/10.1016/j.jmatprotec.2018.08.043> (2019).
28. K. Hoefler and P. Mayr, *Mater. Sci. Forum* 941, 2137 <http://doi.org/10.4028/www.scientific.net/MSF.941.2137> (2018).
29. J.G.M. Rojas, M. Ghasri-Khouzani, T. Wolfe, B. Fleck, H. Henein, and A.J. Qureshi, *Int. J. Adv. Manuf. Technol.* 113(5), 1451 <https://doi.org/10.1007/s00170-020-06388-2> (2021).
30. D. Deschuyteneer, F. Petit, M. Gonon, and F. Cambier, *Surf. Coat. Technol.* 283, 162 <https://doi.org/10.1016/j.surfcoat.2015.10.055> (2015).
31. M. Singleton and P. Nash, *Bull. Alloy Phase Diagr.* 10(2), 121 <https://doi.org/10.1007/BF02881419> (1989).
32. P. Bayliss, A.A. Levinson, *Bull. Can. Pet. Geol.* 24(2), 211 (1976). <https://doi.org/10.35767/GSCPBULL.24.2.211>.
33. G. Fisher, D. Crick, J. Wolodko, D. Kichton, L. Parent, *Impact Testing of Materials for Oil Sands Processing Applications* (2007).
34. A. Kagawa, M. Hirata, and Y. Sakamoto, *J. Mater. Sci.* 25(12), 5063 <https://doi.org/10.1007/BF00580130> (1990).
35. J.P. Kruth, L. Froyen, J. Van Vaerenbergh, P. Mercelis, M. Rombouts, and B. Lauwers, *J. Mater. Process. Technol.* 149(1–3), 616 <https://doi.org/10.1016/J.JMATPROTEC.2003.11.051> (2004).
36. D. Gu and Y. Shen, *Mater. Des.* 30(8), 2903 <https://doi.org/10.1016/J.MATDES.2009.01.013> (2009).
37. R. Li, J. Liu, Y. Shi, L. Wang, and W. Jiang, *Int. J. Adv. Manuf. Technol.* 59(9), 1025 <https://doi.org/10.1007/S00170-011-3566-1> (2011).
38. S.A. Khairallah, A.T. Anderson, A. Rubenchik, and W.E. King, *Acta Mater.* 108, 36 <https://doi.org/10.1016/J.ACTA MAT.2016.02.014> (2016).
39. D. Gu, H. Wang, and G. Zhang, *Metall. Mater. Trans. A Phys. Metall. Mater. Sci.* 45(1), 464 <https://doi.org/10.1007/S11661-013-1968-4/FIGURES/12> (2014).
40. A. Kolsgaard and S. Brusethaug, *Mater. Sci. Technol.* 10(6), 545 <https://doi.org/10.1179/mst.1994.10.6.545> (1994).
41. N.S. Cheng and A.W.K. Law, *Powder Technol.* 129(1–3), 156 [https://doi.org/10.1016/S0032-5910\(02\)00274-7](https://doi.org/10.1016/S0032-5910(02)00274-7) (2003).
42. D. Gu and Y. Shen, *Appl. Surf. Sci.* 255(5, Part 1), 1880 <https://doi.org/10.1016/j.apsusc.2008.06.118> (2008).
43. R. Li, J. Liu, Y. Shi, L. Wang, and W. Jiang, *Int. J. Adv. Manuf. Technol.* 59(9), 1025 <https://doi.org/10.1007/s00170-011-3566-1> (2012).
44. A.I.H. Committee, *ASM Handbook Volume 15: Casting* (ASM International, Materials Park, 2010), p. 470.
45. C.L. Yaws, *Yaws' Handbook of Thermodynamic Properties for Hydrocarbons and Chemicals* (Knovel, Beaumont, 2009), p164.
46. J.J. Licari and D.W. Swanson, *Adhesives Technology for Electronic Applications—Materials, Processing, Reliability* (Elsevier, Waltham, 2011), pp. 56–57.
47. R.M. German and A. Bose, *Binder and Polymer Assisted Powder Processing* (ASM International, Materials Park, 2020), p224.

48. S. Zhao, C. Jia, Y. Yuan, L. Wang, Y. Huang, and L. Yang, *Int. J. Refract. Met. Hard Mater.* 103, 105720 <https://doi.org/10.1016/J.IJRMHM.2021.105720> (2022).
49. Q. Li, T.C. Lei, and W.Z. Chen, *Surf. Coat. Technol.* 114(2–3), 285 [https://doi.org/10.1016/S0257-8972\(99\)00056-0](https://doi.org/10.1016/S0257-8972(99)00056-0) (1999).
50. S. Zhao, L. Yang, Y. Huang, and S. Xu, *Addit. Manuf.* 38, 101738 <https://doi.org/10.1016/J.ADDMA.2020.101738> (2021).
51. R.J. Arsenault and M. Taya, *Acta Metall.* 35(3), 651 [https://doi.org/10.1016/0001-6160\(87\)90188-X](https://doi.org/10.1016/0001-6160(87)90188-X) (1987).
52. S. Ho and E.J. Lavernia, *Appl. Compos. Mater. Int. J. Sci. Appl. Compos. Mater.* 2(1), 1 <https://doi.org/10.1007/BF00567374/METRICS> (1995).
53. Y.N. Picard, *Scanning Electron Microscopy* (ASM International, 2019) <https://doi.org/10.31399/asm.hb.v10.a0006668>.
54. P.Q. Xu, J.W. Ren, P.L. Zhang, H.Y. Gong, and S.L. Yang, *J. Mater. Eng. Perform.* 22(2), 613 <https://doi.org/10.1007/S11665-012-0279-Z/FIGURES/11> (2013).
55. Q. Wang, Q. Li, L. Zhang, D.X. Chen, H. Jin, J.D. Li, J.W. Zhang, and C.Y. Ban, *Ceram. Int.* 48(6), 7905 <https://doi.org/10.1016/J.CERAMINT.2021.11.338> (2022).
56. S. Ilo, C. Just, E. Badisch, J. Wosik, and H. Danninger, *Mater. Sci. Eng., A* 527(23), 6378 <https://doi.org/10.1016/J.MSEA.2010.06.060> (2010).
57. A.I.H. Committee, *ASM Handbook, Volume 05—Surface Engineering* (ASM International, Materials Park, 1994), p. 471.

Publisher's Note Springer Nature remains neutral with regard to jurisdictional claims in published maps and institutional affiliations.

Springer Nature or its licensor (e.g. a society or other partner) holds exclusive rights to this article under a publishing agreement with the author(s) or other rightsholder(s); author self-archiving of the accepted manuscript version of this article is solely governed by the terms of such publishing agreement and applicable law.